minerals

Article

Tectonic-Thermal Evolution of the Wadi El-Dahal Area, North Eastern Desert, Egypt: Constraints on the Suez Rift Development

Sherif Mansour [1], Noriko Hasebe [2], Mohamed Zaki Khedr [3,*], Akihiro Tamura [4] and Amer A. Shehata [1,5]

[1] Geology Department, Faculty of Science, Port Said University, Port Said 42522, Egypt; sherif@sci.psu.edu.eg (S.M.); amer_esmail@sci.psu.edu.eg (A.A.S.)
[2] Institute of Nature and Environmental Technology, Kanazawa University, Kanazawa 920-1192, Japan; hasebe@staff.kanazawa-u.ac.jp
[3] Geology Department, Faculty of Science, Kafrelsheikh University, Kafr El Sheikh 33516, Egypt
[4] Department of Earth Sciences, Kanazawa University, Kanazawa 920-1192, Japan; aking826@staff.kanazawa-u.ac.jp
[5] Department of Physical and Environmental Sciences, College of Science, Texas A&M University-Corpus Christi, 6300 Ocean Drive, Corpus Christi, TX 78412, USA
* Correspondence: mohamed.khader1@sci.kfs.edu.eg; Tel.: +20-10-1301-7715

Abstract: The Suez Rift developed as a northern extension of the Red Sea rift during the Oligocene-Miocene, whose flanks were constructed from the Neoproterozoic basement rocks of the Arabian–Nubian Shield. These basement rocks are comprised of the whole tectonic history since their formation. The Suez Rift initiation model and proposed thermal overprint role in the rifting process and flank development remain uncertain. Additionally, the amplitude of different regional tectonic events' effects on the region is still debatable. Integration of fission-track thermochronology data with modeling of the time-temperature history has demonstrated efficiency in addressing such issues. In the context of this study, eleven representative samples were collected from the different rock units in the Wadi El-Dahal area at the northern tip of the western flank of the Suez Rift. These samples revealed Carboniferous zircon fission-track cooling ages of 353 ± 9 Ma and 344 ± 11 Ma. Meanwhile, the apatite fission-track analysis provided two spatially separated age groups: Permian-Triassic and Late Cretaceous, with average ages of 249 ± 11 Ma and ca. 86 ± 10 Ma, respectively. The time-temperature modeling revealed four possible cooling pulses representing exhumation events, which were initiated as a response to four tectonic activities: the accretion-subsequent event of erosion during the Neoproterozoic, the Hercynian (Variscan) tectonic event during the Devonian-Carboniferous, the Mid-Atlantic opening during the Cretaceous, and the Suez Rift opening during the Oligocene-Miocene. The western flank of the Suez Rift suggests a passive mechanical type with no extra thermal overprint, as indicated by the dominance of older thermochronological ages, modest rift flank elevations, and a reduction in the heat flow.

Keywords: Egyptian Eastern Desert; thermochronology; Arabian-Nubian Shield; fission-track; the Gulf of Suez; mantle plume

check for updates

Citation: Mansour, S.; Hasebe, N.; Khedr, M.Z.; Tamura, A.; Shehata, A.A. Tectonic-Thermal Evolution of the Wadi El-Dahal Area, North Eastern Desert, Egypt: Constraints on the Suez Rift Development. *Minerals* **2023**, *13*, 1021. https://doi.org/10.3390/min13081021

Academic Editor: José Javier Alvaro

Received: 14 June 2023
Revised: 16 July 2023
Accepted: 28 July 2023
Published: 30 July 2023

1. Introduction

The Gulf of Suez represents the northern extension of the Red Sea rift system, which is a continental lithospheric rift that developed partially into a seafloor spreading stage in its southern portion [1]. The rifting processes can be studied indirectly through the rift flanks, as any rift-accompanied activity, volcanism, and/or thermal effect will be printed on the rift shoulders [2,3]. The Suez Rift flanks are constructed from Neoproterozoic Arabian-Nubian Shield (ANS) basement rocks (Figure 1). The ANS was initially established between ca. 900–650 Ma as part of the northern activities of the East African Orogeny (EAO) [4–8]. The ANS in the North Eastern Desert (NED) and Sinai are equivalent, dominated by post-tectonic (ca. 622–535 Ma; [8]) younger granitoids, dike suits, and volcano-sedimentary succession exposures, and lesser existence of the older granitoids (ca. 753–733 Ma; [8]) and ophiolites [2,8–15].

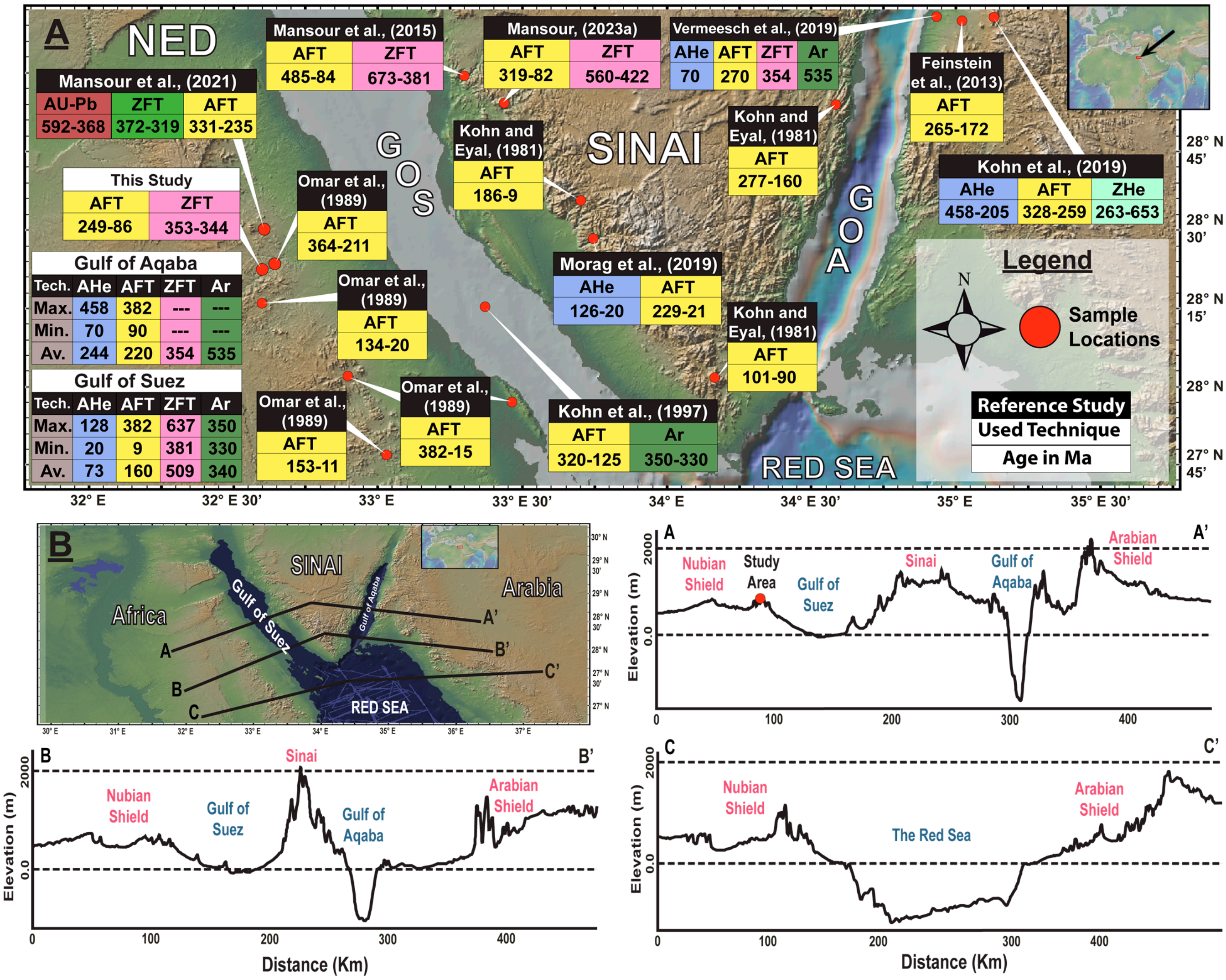

Figure 1. (**A**) Location map for the northern ANS, representing the current study sampling location and previous thermochronological studies (modified after [2]). Where ZFT = zircon fission-track, ZHe; zircon (U-Th)/He, Ar = Ar-Ar dating; AFT = apatite fission-track, and AHe; apatite (U-Th)/He [2,3,16–22]. (**B**) Locations of the represented topographic cross sections (A-A′, B-B′, C-C′).

After growth during the Ediacaran [8], the Egyptian ANS (ENS) was completely eroded by the Cambrian time, marked by the development of a peneplain surface [23]. Afterward, a ca. 2.5 km thickness of Lower Paleozoic aged sedimentary succession accumulated [24]. This regime was interrupted by the Devonian-Carboniferous activated Hercynian (Variscan) tectonic event, which caused a sequence of uplifts and erosions in the region [25]. Then, a thermo-tectonic stability phase dominated until the Cretaceous [26], when the Mid-Atlantic initiation affected the region by faulting, folding, and development of the Syrian arc system [27–29]. Shortly after, the northern Red Sea/the Suez Rift, initiated by the Oligocene-Miocene, developed grabens at the rift axis and elevated flanks [30,31].

Reconstruction of the tectonic-thermal history of the northern Red Sea/Gulf of Suez Rift and its Neoproterozoic ANS basement flanks (Figure 1) can be achieved by integrating different thermochronological techniques with time-temperature modeling [32,33]. Several thermochronological studies have taken place on the rift system flanks of the Red Sea, the Gulf of Aqaba, and the eastern Gulf of Suez [2,3,16,19,20,22,24,34–39], whilst less attention was given to the western flank of the rift [17,18]. This information shortage is responsible for several uncertainties in concern to the tectonic development of the region. In particular, the northern Red Sea/Gulf of Suez Rift type, the existence/absence of any thermal overprint that accompanied the rifting process, the regional tectonic events that affected the area of study, and the reason behind the heterogeneity of the rift elevated flanks through its different segments (Figure 1B). There is debate about the type of the northern Red Sea/Gulf of Suez Rift and the proposed existence of an additional thermal overprint. One model suggested a rift with a mechanical component where the flanks were exhumed by an isostatic rebound to rift axis development [18,37]. A second model considered an additional Sinai triple junction thermal effect [34,40]. A third model recommended the role of the proposed Cairo mini mantle plume [3,41]. Furthermore, a northward extension of the Afar plume towards the Arabian plate margin has been reported [42,43]. This could provide a more localized source from the Afar plume through lateral migration of melts [41,44].

Low-temperature thermochronology techniques have proven to be powerful tools to address the aforementioned issues [2,3,16–18,32,45]. Therefore, reconstructing the thermal-tectonic history of the area of study, which represents the ANS basement rocks in the Egyptian North Eastern Desert and central western flank of the Suez Rift (Figure 2), will provide new insights into the regional tectonic events that affected the area of study and to what extent and, furthermore, the role of Sinai triple junction or a mantle plume effect in the Suez Rift initiation. This role can be detected through their accompanying thermal anomaly.

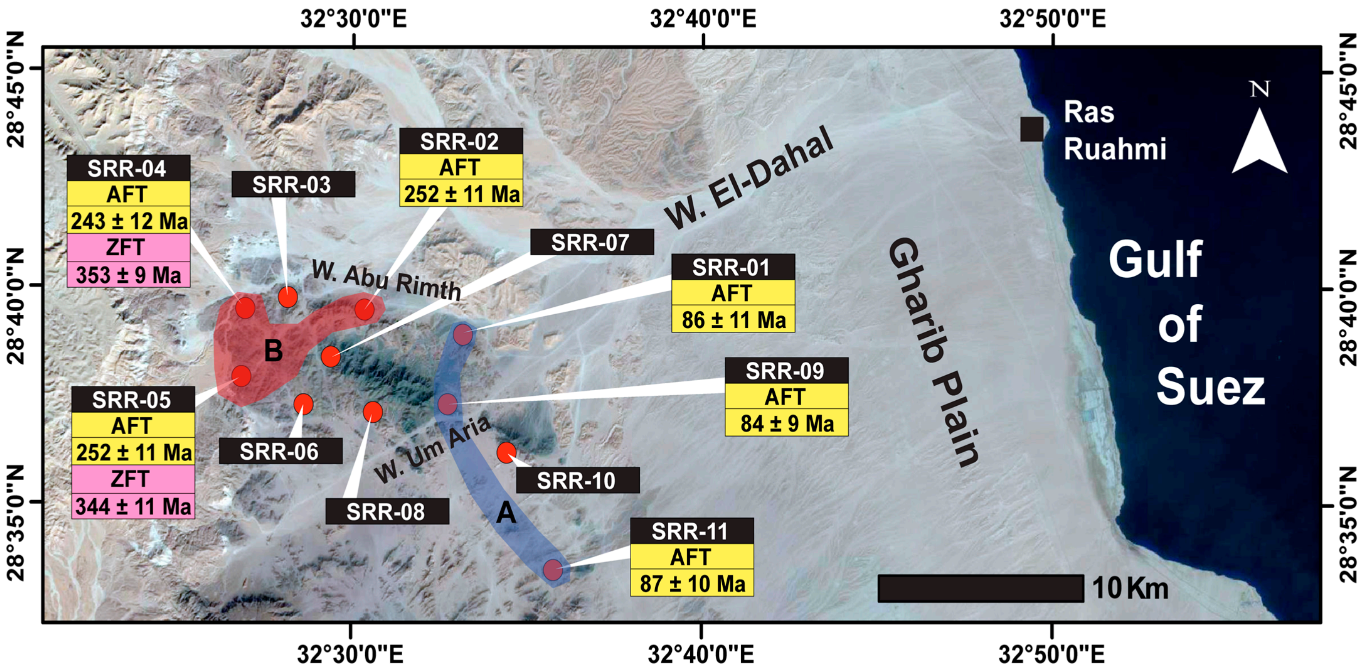

Figure 2. A Landsat8-based location map for the Wadi El-Dahal area where locations of the dated samples are represented.

A better understanding of the tectonic history of the Gulf of Suez could additionally help the efforts of assigning the tectonic-climatic relationship [46–49], evaluating the tectonically shaped hydrocarbon basins [50–52], delineating structurally controlled aquifers in Egypt [53–55], and assessing the geohazards in the newly developed cities within the Gulf of Suez region [56,57].

2. Geologic Setting

The Red Sea/Gulf of Suez Rift system initiation was triggered by the Afar superplume activities by ca. 34 Ma [58–61], along with the Bitlis-Zagros subduction and the following convergence zone in modern Anatolia [62,63]. The first (ca. 45 Ma) and second (31–29 Ma) voluminous volcanisms in the Afar triple junction were focused along its vicinity at Kenya, Ethiopia, and Yemen [44,64–67]. Then, this activity migrated further north by ca. 28 Ma, forming the Older Harrats along the Arabian western margin [66]. Afterward, volcanisms and dike swarms activated along the western margin of Arabia by 24–21 Ma, which are chemically comparable to the Afar plume [66]. These magmatic activities were accompanied by a main extensional event (24 ± 2.2 Ma) propagating northward through the rift [37,38,68–70]. As a consequence, elevated flanks formed along the central and northern Red Sea [3,17,18,20,35,45]. Then, a second flank uplift phase (ca. 15 Ma) was recorded in central Arabia [45]. Shortly after, additional volcanic activity began (ca. 13 Ma) in western Arabia, forming the Younger Harrats [1].

The whole Red Sea rift system Is flanked by the basement rocks of the ANS, which were initially formed by mass accumulation of continental fragments, island arcs, and oceanic plateaus during the EAO in the time span from ca. 900 to and 650 Ma [6,8]. These basement rocks in Egypt are constructed mainly of (1) the island arc suite representing the EAO's oldest activity that prolonged between ca. 820 Ma and 750 Ma [8,71], (2) the syn-orogenic alkaline and calc-alkaline granitoid suite characterizing the EAO compressional stage that extended from ca. 750 to 610 Ma [8,72,73], (3) the post-orogenic calc-alkaline and alkaline granitoid and dike swarm suites representing the EAO extensional phase that dominated from ca. 610 Ma and 535 Ma [8,72,74,75], and (4) the ophiolites and metamorphic complexes [72,75].

After the EAO, a post-accretion event of intense erosion (PAEE) entirely removed the ANS high topography before the Cambrian time. This has been documented by identifying fossils with a Lower Cambrian age in sediment with near-shore marine to fluvial affinity [63,76]. These sediment accumulations were sustained until the Devonian and deposited more than a 2.5 Km sequence of a pre-Carboniferous age. While by the Devonian-Carboniferous time, the Hercynian (Variscan) tectonic activity developed by suturing of the Gondwana with the Laurasia [25]. This collision initiated significant uplifts and erosions in the Lower Paleozoic sequence of the NED and Sinai [2,17,38,77–79]. Meanwhile, a complete succession was conserved in South Jordan and North Saudi Arabia [24,80]. By the Jurassic-Cretaceous time, the Gondwana breakup began affecting northern Egypt via sinistral shearing, localized volcanic activity, and the Syrian Arc system [27–29,81,82]. By the Oligocene-Miocene time, the northern Red Sea/the Suez Rift system began producing elevated rift flanks, restricted basic dykes, and normal faults.

The area of study represents the northwestern termination of the exposed ANS basement rocks in the Egyptian Eastern Desert. It is identified by a lack of high elevations when compared to the southeastern exposures of the Gulf of Suez's eastern flank, located directly on the western border of the rift, far from the Sinai triple junction and/or the Gulf of Aqaba initiation activities (Figure 1). Lithologically, it is constructed of Neoproterozoic basement rocks; consequently, all sampled rocks preceded the whole Phanerozoic tectonic events. The area of study is relatively small, which enables analyzing many samples close to each other to examine the previously reported thermochronologic age-wide distribution in the ANS (Figure 1). This strategy would limit the possibility of a heat flow differentiation between the different parts of a small region, making the tectonic effect the main factor responsible for any thermochronological age differentiation (Figure 2).

3. Methods and Techniques

The fission-track, low-temperature thermochronology technique is based on radiation damage (etchable tracks) of the spontaneous ^{238}U fission accumulation in the crystal lattice [83]. The retention and annealing of these tracks of fission are sensitive to a temperature zone that varies with different minerals [84,85], which enables thermal-tectonic (t-T) history reconstruction.

FT counting and horizontally confined track (CT) length measurements were performed using a Nikon Eclipse 80i (Nikon Solutions Co., Ltd., Tokyo, Japan) upgraded with a digital camera, image processing software, and dry objectives at the thermochronology laboratory of Kanazawa University, Kanazawa, Japan. Analyses of both apatite-fission-track (AFT) and zircon-fission-track (ZFT) were conducted using the Laser Ablation Inductively Coupled Plasma Mass Spectrometry (LA-ICP-MS) technique of Kanazawa University. The LA-ICP-MS technique enables measuring the U concentrations directly [86]; the operating conditions are illustrated in Table 1 [87]. The zircon mounts were etched in a eutectic melt of NaOH–KOH at 220 ± 5 °C [88] for 50–75 min. Meanwhile, the apatite mounts were etched for 20 s in 5.5 N HNO_3 at 20 ± 1 °C [50]. The weighted mean cooling ages and error ranges for both minerals were calculated using IsoplotR [89].

Table 1. LA-ICP-MS operation conditions.

ICP-MS	
Model	Agilent 7500s
Forward power	1200 W
Reflected power	1 W
Carrier gas flow	1. 31/min (Ar), 0.31/min (He)
Auxiliary gas flow	1.01/min
Plasma gas flow	151/min
Interface	Ni sample cone, Ni skimmer cone
Laser	
Model	MicroLas GeoLas Q plus
Wavelength	193 nm (Excimer ArF)
Repetition rate	5 Hz
Pulse energy	8 J/cm^2
Pit diameter	20 µm

The intensity of the Uranium signal was calibrated against the silicate glass reference material SRM 610 produced by the National Institute of Standards and Technology (NIST 610) [90], in which the ^{238}U concentration was 456 ppm [91,92]. ^{43}Ca was used as an internal standard for apatites, using chemical data obtained previously [93]. Meanwhile, ^{29}Si was the internal standard and tracked the chemical composition for zircons [90,92].

Thermal history reconstruction was performed by the modeling program HeFTy v1.9.1 [94]. The constraints guiding the Monte-Carlo algorithm were chosen as initial constraints with the Neoproterozoic age (at depth), near-surface between the Neoproterozoic and the Cambrian (the PAEE), ZFT ages (whenever measured), AFT ages, and the rift initiation age. Models were run with 500,000 iterations. Each t-T path in HeFTy was described by a goodness of fit (GOF) rate that indicated its fit-nearness to the measured inputted data. All t-T paths with <0.05 GOF did not appear in the model; ≥0.05 (≥5%) rates were accepted models and presented in green, and ≥0.5 (≥50%) rates were good models represented in purple in the model. Additionally, the code calculated the best GOF model and displayed it in black, and the model with the weighted mean value was displayed in blue [94,95].

Thermochronology techniques measure cooling age, which can be produced either by exhumation (rock uplifted to shallower and cooler depths) or a change in heat flow. Therefore, not all cooling is necessarily related to rock uplift; however, we study here plutonic rocks which were formed deep in the crust and are today on the surface. This means that these rocks were exhumed throughout their history until reaching the surface. Despite being precise fission-track and thermal history modeling techniques within the error range as any other dating technique, we always interpreted our results with a wide range, such as a Devonian-Carboniferous or a Cretaceous event. Furthermore, we did not use our thermochronological data alone; it was always supported by other data (i.e., tectonic history and sedimentologic record). Additionally, the area of study was relatively small, which enabled analyzing many samples close to each other to examine the conventionally reported thermochronological age-wide distribution in the ANS (Figure 1). This strategy limited the possibility of heat flow differentiation between the different parts of that small region as a reason for age differentiation, making structurally controlled tectonic effects the main factor responsible for thermochronologic age differentiation. Despite that, we still took the heat flow change possibility into consideration by using a wide range of geothermal gradients. We did not interpret our thermochronological data and the corresponding t-T models as an exhumation expression, except when we had other supporting data. So, essentially, we had a wide age range (for the age corresponding to a tectonic event) and wide exhumation amount (for wide geothermal gradient possibility ranges between 25–50 °C/km), and then compared our findings to the regional geological history, as we will illustrate later. In the case of raising unknowns other than the geothermal gradient (i.e., emplacement depths), we did not even make assumptions for the amount of exhumation.

Cooling and uplifting rates and the event-related rock exhumations were inferred from our thermochronological ages, and the t-T major pattern changes through temperature cooling between the different thermochronometers (ZFT and AFT) and the surface. Also, two possibilities of geothermal gradients (25 or 50 °C/km; [21,35,96]) were used for exhumation rate calculations because no specific paleo-geothermal gradient values have been reported. Hereafter, the obtained values were compared to the reported sedimentological data and the regional tectonic history.

For this study, we collected eleven basement rock samples from the central Suez Rift's western flank (Figure 2). These samples belonged to the different ANS rock units represented in the area of study, which comprised the entire geologic history of the region from its development during the EAO until the Suez Rift development. The dated minerals were separated through the conventional methods that were illustrated by Donelick et al. [97].

4. Results and Discussion

From the 11 analyzed samples, two samples provided appropriate zircon grains for ZFT analyses (Table 2), and six samples provided appropriate apatite grains for AFT analyses (Table 3). Out of the dated six AFT samples, two provided an appropriate amount of horizontal confined tracks (HCTLs) for thermal history modeling.

Table 2. Detailed fission-track data, ages, and sample descriptions for the dated zircons.

S.-Code	Elev.	Coordinates Decimal		Lithology	^{238}U	n	ρ_s	N_s	χ^2 [%]	Age [Ma]		
		N	E		[μg/g]		($\times 10^6$ track/cm^2)			W.M.	1σ	MSWD
SRR-04	478	28.66313°	32.44926°	Diorite	343.8	18	68.4	5433	0.89	**352.8**	9.3	0.61
SRR-05	604	28.62544°	32.44434°	Monzogranite	360.5	15	69.0	4260	0.90	**343.6**	10.5	0.56

Samples and zircon fission-track data represented as W.M.; weighted mean ages with 1-sigma (σ) uncertainties, calculated with IsopltR [89]. S.-Code; samples code, Elev.; the elevation above sea level of each sample in meters, U; concentration of ^{238}U in μg/g, n; the number of apatites where tracks were counted, ρ_s; spontaneous tracks densities (10^6 tr/cm^2), N_s; the number of counted fission tracks, χ^2; chi-square test values, MSWD; Mean Sum Weighted Deviates.

4.1. Zircon Fission-Track Thermochronometry

The statistical Chi-square (χ^2) test for age homogeneity was passed by each of the examined samples, representing no evidence for several age populations (Table 2). Uranium concentrations in our zircons were of ca. 361 and 344 μg/g (Table 2). The correlation between single grains ZFT ages and the corresponding uranium concentrations was absent (correlation value = −0.0156), taking into account the Th content of lesser effect, indicating that the metamictization effect could be neglected (Figure 3).

Table 3. Apatite fission-track age details, sample descriptions, and track length data.

S.-No.	Elev.	Coordinates Decimal N	Coordinates Decimal E	Lithology	^{238}U [μg/g]	n	ρ_{σ} (×10^6 track/cm^2)	N_s (×10^6 track/cm^2)	χ^2 [%]	W.M. Age [Ma]	1σ [Ma]	Age MSWD	CTs (μm)	SD (μm)	Dpar (μm)	SD (μm)
							Group A									
SRR-01	391	28.64418°	32.55747°	Diorite	7.1	20	0.3	238	1.00	**86.1**	10.5	0.08	**10.6**	2.5	**1.7**	0.1
SRR-09	494	28.61221°	32.53076°	Dacite	6.2	22	0.3	88	1.00	**84.1**	9.3	0.03	NA	NA	NA	NA
SRR-11	416	28.57803°	32.57923°	Monzogranite	6.8	20	0.3	74	1.00	**87.3**	10.4	0.02	NA	NA	NA	NA
							Group B									
SRR-02	469	28.65925°	32.50880°	Monzogranite	22.0	21	3.0	939	0.98	**252.3**	10.5	0.45	NA	NA	NA	NA
SRR-03	455	28.66721°	32.47174°	Granite	NA	NA	NA	NA	NA	NA	NA	NA	NA	NA	NA	NA
SRR-04	478	28.66313°	32.44926°	Diorite	19.1	17	2.5	611	0.98	**242.9**	12.3	0.40	NA	NA	NA	NA
SRR-05	604	28.62544°	32.44434°	Monzogranite	20.0	21	2.8	880	0.99	**252.4**	10.9	0.43	**10.1**	2.0	**1.5**	0.1
SRR-06	562	28.61681°	32.48201°	Diorite	NA	NA	NA	NA	NA	NA	NA	NA	NA	NA	NA	NA
SRR-07	591	28.64358°	32.48344°	Dacite	NA	NA	NA	NA	NA	NA	NA	NA	NA	NA	NA	NA
SRR-08	462	28.61841°	32.50517°	Diorite	NA	NA	NA	NA	NA	NA	NA	NA	NA	NA	NA	NA
SRR-10	478	28.60291°	32.57185°	Dacite	NA	NA	NA	NA	NA	NA	NA	NA	NA	NA	NA	NA

Sample information and apatite fission-track data given as weighted mean ages with 1-sigma (σ) uncertainties, calculated with IsopltR [89], CTs mean, mean confined track lengths; Dpar, mean etch pit diameter; NA, not applicable. The collected samples belong to the syn- and post-orogenic alkaline and calc-alkaline granitoid suites [8]. More details are provided in Table 2.

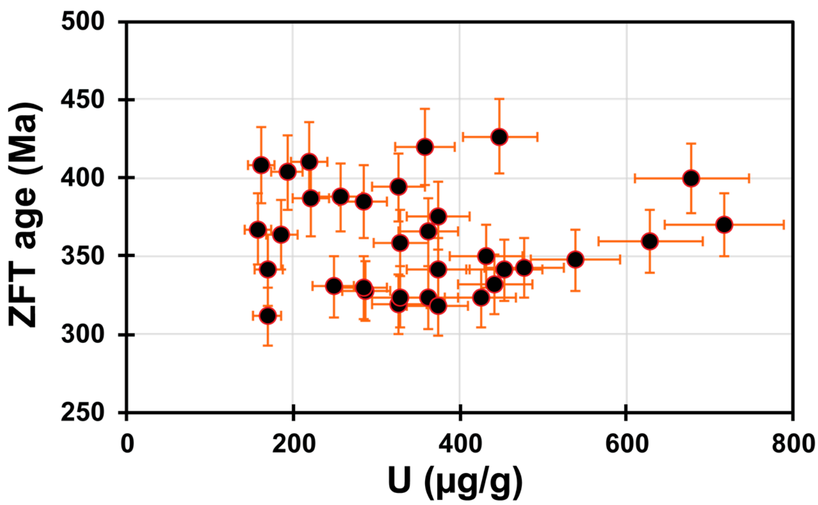

Figure 3. A ZFT ages against ^{238}U concentrations plot, representing the absence of any systematic pattern and any Metamictization effect on the calculated ZFT ages.

The resulting ZFT weighted mean ages and the corresponding 1σ of standard errors were 353 ± 9 Ma and 344 ± 11 Ma (Figure 2), demonstrating cooling through the PAZ of ZFT thermochronometer (240–200 °C; [98]) ca. 348 ± 10 Myrs ago. These ages are consistent with the published ZFT ages from other regions in the ANS, which were countered for a tectonic-induced differential exhumation during the Devonian-Carboniferous [21,24,38]. This uplift is also consistent with the regional stratigraphic sequence that suggested the previous existence and erosion of more than 2.5 km of the Lower Palaeozoic succession [25,99]. The accompanied uplift was emphasized by changing the depositional regime to completely nonmarine sediments during the Upper Carboniferous [78,100].

4.2. Apatite Fission-Track Thermochronometry

The treated AFTs had ages ranging from 252 ± 11 Ma to 84 ± 9 Ma. These periods could be differentiated into two discrete age categories (Table 3); Group A contained 3 samples with Permo-Triassic ages ranging between 252 ± 11 Ma and 243 ± 12 Ma (Figure 2), documenting cooling through/to the PAZ of the AFT (110–60 °C; [97,101]) at ca. 249 ± 12 Ma (Figure 2; Table 3). These ages are concurrent with multiple unconformities between the synchronously Permian basaltic volcanism and successive deposited sedimentary formations with terrestrial nature (Qiseib and Malha formations) in the region [102,103]. Additionally, similar cooling ages were reported from other localities of the ANS [3,16,18,22,35]. While Group B consisted of three samples with Late Cretaceous ages ranging between 87 ± 10 Ma and 84 ± 9 Ma, suggesting cooling to the PAZ temperatures of the AFT technique at ca. 86 ± 11 Ma (Figure 2; Table 3), these ages are simultaneous with the sedimentological depositional regime conversion from the non-terrestrial Wata Formation to the terrestrial Matulla Formation [102,103], suggesting a possible uplift. Furthermore, comparable cooling ages have been described in other ANS regions [3,16–18,22,35,38,99].

The spatially separated nature of the AFT age groups suggests a differential thermo-tectonic-related exhumation that was characterized by localized block movement through bounding faults (Figure 4). This uplifting nature was earlier reported from other parts of the ANS [16,18–21,35,99]. We suggest that the response of the studied area to each tectonic event was controlled by the accompanying direction of stress.

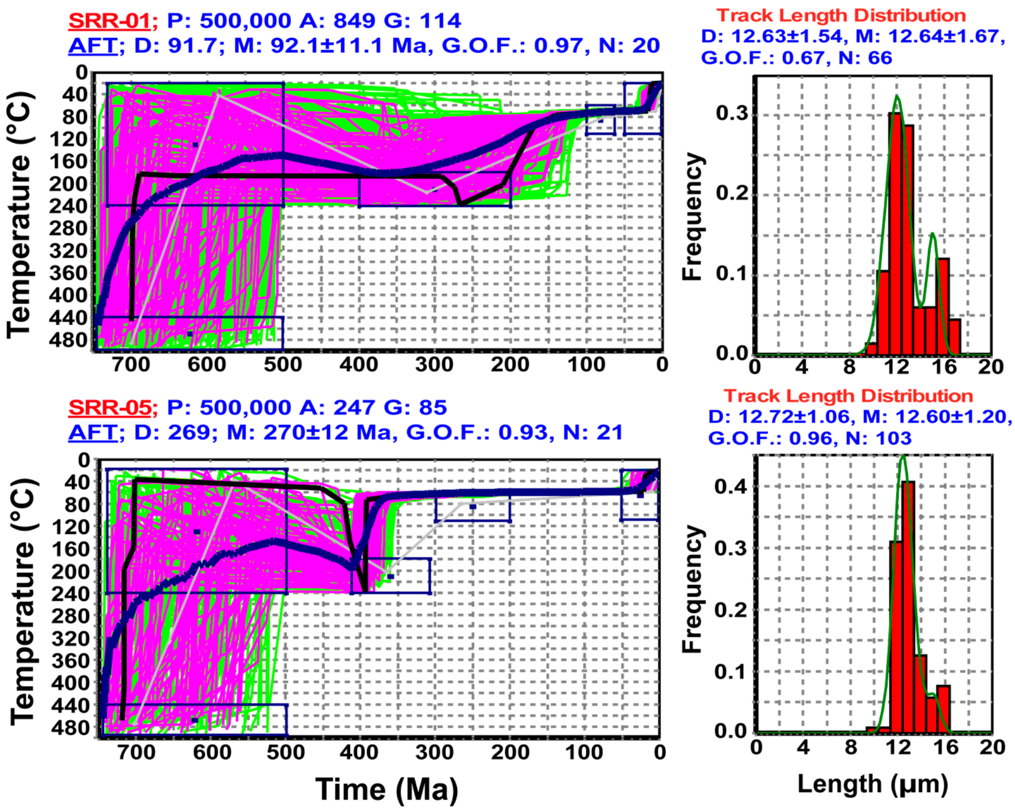

Figure 4. Thermal history models reconstructed using the HeFTy code [104]. The resulting t-T paths represent four levels of reliability; acceptable fit (green), good fit (purple), the best fit (black), and the weighted mean (blue) paths [95,104]. Five constraints were used to limit the modeling randomness, where the 1st represented the initial box at depth, the 2nd represents the post-accretion-related exhumation event, the 3rd shows the ZFT age, the 4th shows the AFT age, and the 5th represents the Suez Rift opening. Where SRR-01: sample code, P: number of inverse iterations, A: acceptable fit models' number, G: good fit models' number, D: calculated AFT ages and CLs (1-σ error), M: model calculated AFT ages and CLs, G.O.F.: goodness of fit, N: number of single grains and CLs.

The obtained AFT cooling ages did not reset during the Oligocene-Miocene rift-related exhumation event (the youngest AFT age is ca. 84 Ma), an indication of exhumation from the AFT PAZ. In other words, the rift flanks in the area of study have not acknowledged any temperatures greater than 110 °C (AFT closure temperature) since the Late Cretaceous. Furthermore, the correlation between AFT cooling ages and horizontal mean track lengths (Figure 5) from this study and previous regional thermochronological studies [3,16,18,19] defines two main trends. First, a negative correlation for samples with AFT ages younger than 55 Ma, which suggests samples' exhumation from near the AFT PAZ base, and annealing of the pre-uplift formed tracks [101]. Secondly, a general positive correlation for samples with older AFT ages (Figure 5) indicates samples' exhumation from within the AFT PAZ and variable degrees of partial annealing for pre-uplift tracks [101]. Therefore, the obtained cooling ages are marginally older than the cooling/uplifting events that resulted in them, indicating a lengthy stay in the PAZ upper portion of the AFT technique. This is further supported by the track lengths distribution histograms and t-T models, as the majority of unprojected confined tracks and the c-axis projected confined tracks (Lc) exhibit positive skewness values and a tail of longer tracks (Figure 4).

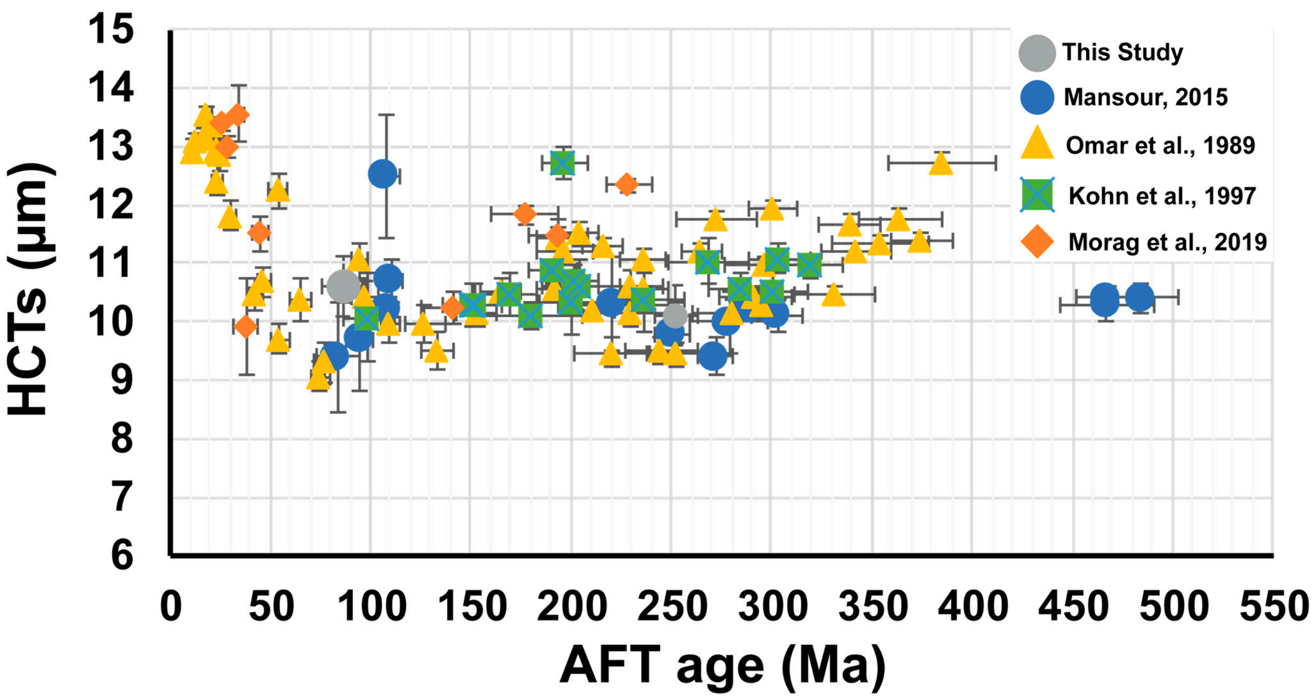

Figure 5. Mean track length vs. AFT age plot for samples from this study and previous thermochronological studies (i.e., [3,16,18,19]).

4.3. Thermal History Modelling

The time-temperature (t-T) history was reconstructed using the code of HeFTy [94]. The Monte Carlo algorithm in HeFTy is guided by user-defined t-T constraints. We defined these constraints according to the calculated cooling ages (AFT and ZFT) and the previously reported geologic events: the Precambrian post-assembly event of erosion (PAEE), when the whole Egyptian portion of the ANS was eroded, and initiation of the northern Red Sea/Suez Rift during the Oligocene-Miocene (Figure 4). According to the degree of uncertainties of each event, the extent of these boxes on the time axis was modified. When the ZFT age was not obtained, a corresponding wide constraint was built to offer a greater degree of liberty. The precision of the modeled thermal histories was highly dependent on the HCTLs abundance. Thus, the t-T histories were only modeled when adequate numbers of HCTLs were measured (Table 3).

The t-T models recommend an initial rapid exhumation event during the Precambrian to uplift rocks nearer to the surface. This uplifting event was caused by the PAEE, which completely eroded the ENS basement before the Cambrian time. However, the position of the recent rock exposures during the Cambrian is unknown as they might have been exposed to the surface or buried in the subsurface. Unfortunately, the t-T models could not provide exclusive answers. Afterward, the study area experienced a burial/reheating event beneath a Lower Paleozoic sedimentary sequence until the Devonian-Carboniferous (Figure 4). Then, a Devonian-Carboniferous rapid cooling event occurred, causing uplifting to the AFT PAZ. This was the regional reaction to the Hercynian (Variscan) event, causing the elimination of more than 2.5 km of the Lower Palaeozoic sedimentary sequence and an additional amount from the fundamental basement rocks [79]. This uplift is marked sedimentologically by changing the sedimentation environment from the marine Lower Carboniferous aged formation of Um Bogmato to the terrestrial Upper Carboniferous formation of Abu Darag [102,103]. Additionally, there is no record of major Late Palaeozoic magmatism in the region that may have provided additional thermal sources or, rather, uplift and erosion [17,38,77,99,105]. Further, the model of sample SRR-01 represents a possible overprinting of a Cretaceous cooling event on the Devonian-Carboniferous event (Figure 4). This possibility of a Cretaceous event is supported by this sample (SRR-01) being representative of the younger AFT Late Cretaceous age group, pauses, and the erosional deposits' predominance during the Cretaceous [102,103]. This event recommends differential rock uplift as previously reported through thermochronological studies [16–18,20–22,24,35]. This event was initiated as a response to the Mid-Atlantic opening, which caused localized rock uplifts in the Suez Rift vicinity [16,99], the whole of northern Africa, and tectonically driven strike-slip faults [22,38]. Afterward, the region was dominated by a slow cooling regime until the Oligocene-Miocene time (Figure 4). Then, the northern Red Sea/Gulf of Suez Rift system began, and the corresponding flanks were exhumed. The un-reset AFT ages (Table 3) indicate exhumation from depths greater than ca. 110–60 °C temperatures, while the thermal history models restrict this to depths corresponding to ca. 60 °C (Figure 4).

4.4. Cooling and Uplifting Events

The cooling events associated with rock exhumation could be calculated from the obtained cooling ages, the thermochronometer PAZ, and the t-T models. Here, due to the absence of precise paleo-geothermal gradients, we used a range of geothermal gradients between the current (25 °C/km) and its double, which is expected during active tectonism [18,96]. Then, the calculated values were compared to the lithostratigraphic sequence and the tectonic history of the region.

The sedimentation of near-shore to fluvial sediments with Lower Cambrian fossils [63,76,104] indicates deep erosion for the newly formed ANS and corresponding exhumation as an isostatic rebound. The amount of this exhumation could not be inferred due to a lack of information about the exact timing and depth of emplacement. Then, a Lower Palaeozoic succession of ca. 2.5 km in thickness was deposited [24,78,79]. Afterward, this Lower Palaeozoic succession was completely eroded, except for a few remnants (ca. 350 m) in isolated localities. This removal was triggered by uplifting, as indicated by the changing sedimentation environment from the marine Um Bogma Formation during the Lower Carboniferous to the erosional Abu Darag Formation during the Upper Carboniferous. This means there was an uplift of more than 2.5 km to remove the Lower Palaeozoic succession. This is supported by our t-T modeling, ZFT ages of 349 ± 10 Ma, and the t-T modeling, which suggests a synchronous rock uplift from depths equivalent to the PAZ of ZFT technique (240–200 °C) and temperatures to ca. 60 °C (Figure 4). Our calculations suggest 4.2 ± 1.4 km of accompanied rock uplift, which overlapped with the sedimentologic record. During the Cretaceous, Africa and Eurasia collided during the Gondwana breakup event, and consequently, the Syrian Arc system was developed to affect northern Egypt and caused more than 2.4 km of rock uplift in northern and central

Sinai [105]. This is presented by our older AFT group samples and their t-T models. This event caused the stripping out of any sedimentary cover (Figure 2). Hereafter, the Suez Rift caused rift shoulders to uplift; this uplift raised samples from the AFT PAZ (because the AFT ages did not reset to the Gulf age of ca. 25 Ma), which means presence at depths equivalent to temperatures of less than 110 °C, while our thermal history modeling suggests uplifting from depths corresponding to ca. 60 °C. Even when we examined a higher temperature possibility, the t-T models showed similar temperatures of ca. 60 °C. These temperatures are equivalent to depths of ca. 1.2 ± 0.4 km, which are consistent with the present-day low topography with the highest peak ta ca. 730 m in the area of study, the reported moderate rift-related thermal regime [1,16,19,99], and the expected uplifts based on the non-reset AFT ages, the t-T modeling results, and the HCTLs distribution (Figure 4).

5. Geological History Implications

The calculated cooling ages and reconstructed thermal histories document four cooling/uplifting activities that occurred in response to four events. (1) The Neoproterozoic PAEE, which resulted in a subsequent rocks exhumation through isostatic rebound. The basement rocks column was then reburied beneath more than 2.5 km of a Lower Palaeozoic sedimentary succession. (2) The Devonian-Carboniferous Hercynian (Variscan) tectonic activity, which resulted in rock exhumations of ca. 4.2 ± 1.4 km and elimination of the entire Lower Paleozoic sequence as well as portions of the underlying foundations. (3) The Cretaceous Mid-Atlantic opening event, which likely resulted in a localized uplift as evidenced by the younger AFT age group. (4) The Oligocene-Miocene northern Red Sea/Suez Rift opening, which caused rift shoulders exhumation of more than 1.2 ± 0.4 km. This limited flank uplift, along with pre-rift AFT cooling ages and distribution of the HCTLs, documents the exhumation of rock from PAZ temperatures of the AFT technique. Further, t-T modeling restricts this rift-related rock uplift to depths corresponding to ca. 60 °C (Figure 4). Consequently, we consider the Gulf of Suez to be a mechanical rift (passive) type with additional east-southward thermal overprint caused by lateral migration of melts from the Arabian marginal plume, which caused the 23 Ma basaltic eruptions, southward increase in the heat flow, and the extraordinary southward elevations in southern Sinai (the rift’s eastern flank). In contrast, the rift’s western flank was not affected by this far-field thermal overprint.

6. Conclusions

The resultant zircon fission-track cooling ages have Carboniferous ages of ca. 349 ± 10 Ma and apatite fission-track cooling ages of two spatially separated age groups, the Permian-Triassic (ca. 249 ± 11 Ma) and Late Cretaceous (ca. 86 ± 10 Ma). Integration of these cooling ages and the thermal/tectonic histories modeling revealed four activities that have affected and reshaped the northern segment of the Suez Rift’s western flank: (1) the PAEE, which exhumed rocks from depths of emplacement to nearer the earth’s surface; (2) the Hercynian tectonic event, which caused approximately 4.2 ± 1.4 km of geological uplift in the vicinity; (3) the Mid-Atlantic opening event, which is an imprint of the Hercynian tectonic event in the younger AFT age group region; and (4) the northern Red Sea/Gulf of Suez Rift initiation, which was accompanied by ca. 1.2 ± 0.4 km of rift flanks uplift.

The Suez Rift is a mechanical type of rift with a thermal overprint in the southeast far-field that afflicted the eastern flank. The absence of such a thermal effect on the western flank is supported by the moderate quantity of accompanied exhumation and the resetting of the AFT cooling ages.

Author Contributions: Conceptualization, S.M. and N.H.; methodology, S.M. and N.H.; validation, S.M. and N.H.; formal analysis, A.T. and S.M.; investigation, S.M. and N.H.; resources, M.Z.K. and A.A.S.; data curation, S.M.; writing—original draft preparation, S.M.; writing—review and editing, N.H., M.Z.K. and A.A.S.; visualization, S.M.; supervision, N.H.; project administration, S.M., A.T., M.Z.K. and A.A.S.; funding acquisition, M.Z.K. and A.A.S. All authors have read and agreed to the published version of the manuscript.

Funding: This research received no external funding.

Data Availability Statement: The raw data supporting the conclusions of this article will be made available by the authors without undue reservation.

Acknowledgments: We appreciate the sincere efforts of Mohamed Abdelfattah, Geology Department, Faculty of Science, Port Said University, Egypt, for the fruitful discussions with the first author.

Conflicts of Interest: The authors declare no conflict of interest.

References

1. Boone, S.C.; Balestrieri, M.-L.; Kohn, B. Thermo-Tectonic Imaging of the Gulf of Aden-Red Sea Rift Systems and Afro-Arabian Hinterland. *Earth-Sci. Rev.* **2021**, *222*, 103824. [CrossRef]
2. Mansour, S.; Hasebe, N.; Abdelrahman, K.; Fnais, M.S.; Tamura, A. Reconstructing the Tectonic History of the Arabian–Nubian Shield in Sinai: Low-Temperature Thermochronology Implications on Wadi Agar Area. *Minerals* **2023**, *13*, 574. [CrossRef]
3. Morag, N.; Haviv, I.; Eyal, M.; Kohn, B.P.; Feinstein, S. Early Flank Uplift along the Suez Rift: Implications for the Role of Mantle Plumes and the Onset of the Dead Sea Transform. *Earth Planet. Sci. Lett.* **2019**, *516*, 56–65. [CrossRef]
4. Stern, R.J. ARC Assembly and Continental Collision in the Neoproterozoic East African Orogen: Implications for the Consolidation of Gondwanaland. *Annu. Rev. Earth Planet. Sci.* **1994**, *22*, 319–351. [CrossRef]
5. Kusky, T.M.; Abdelsalam, M.; Tucker, R.D.; Stern, R.J. Evolution of the East African and Related Orogens, and the Assembly of Gondwana. *Precambrian Res.* **2003**, *123*, 81–85. [CrossRef]
6. Meert, J.G. A Synopsis of Events Related to the Assembly of Eastern Gondwana. *Tectonophysics* **2003**, *362*, 1–40. [CrossRef]
7. Elhebiry, M.S.; Sultan, M.; Abu El-Leil, I.; Kehew, A.E.; Bekiet, M.H.; Abdel Shahid, I.; Soliman, N.M.A.; Abotalib, A.Z.; Emil, M. Paleozoic Glaciation in NE Africa: Field and Remote Sensing-Based Evidence from the South Eastern Desert of Egypt. *Int. Geol. Rev.* **2020**, *62*, 1187–1204. [CrossRef]
8. Mansour, S.; Hasebe, N.; Meert, J.G.; Tamura, A.; Khalaf, F.I.; El-Shafei, M.K. Evolution of the Arabian-Nubian Shield in Gabal Samra Area, Sinai; Implications from Zircon U–Pb Geochronology. *J. Afr. Earth Sci.* **2022**, *192*, 104538. [CrossRef]
9. Moghazi, A.M. Geochemistry and Petrogenesis of a High-K Calc-Alkaline Dokhan Volcanic Suite, South Safaga Area, Egypt: The Role of Late Neoproterozoic Crustal Extension. *Precambrian Res.* **2003**, *125*, 161–178. [CrossRef]
10. Eliwa, H.A.; Kimura, J.-I.; Itaya, T. Late Neoproterozoic Dokhan Volcanics, North Eastern Desert, Egypt: Geochemistry and Petrogenesis. *Precambrian Res.* **2006**, *151*, 31–52. [CrossRef]
11. Ali, B.H.; Wilde, S.A.; Gabr, M.M.A. Granitoid Evolution in Sinai, Egypt, Based on Precise SHRIMP U–Pb Zircon Geochronology. *Gondwana Res.* **2009**, *15*, 38–48. [CrossRef]
12. El-Bialy, M.Z. On the Pan-African Transition of the Arabian–Nubian Shield from Compression to Extension: The Post-Collision Dokhan Volcanic Suite of Kid-Malhak Region, Sinai, Egypt. *Gondwana Res.* **2010**, *17*, 26–43. [CrossRef]
13. Eyal, M.; Litvinovsky, B.; Jahn, B.M.; Zanvilevich, A.; Katzir, Y. Origin and Evolution of Post-Collisional Magmatism: Coeval Neoproterozoic Calc-Alkaline and Alkaline Suites of the Sinai Peninsula. *Chem. Geol.* **2010**, *269*, 153–179. [CrossRef]
14. Johnson, P.R.; Andresen, A.; Collins, A.S.; Fowler, A.R.; Fritz, H.; Ghebreab, W.; Kusky, T.; Stern, R.J. Late Cryogenian–Ediacaran History of the Arabian–Nubian Shield: A Review of Depositional, Plutonic, Structural, and Tectonic Events in the Closing Stages of the Northern East African Orogen. *J. Afr. Earth Sci.* **2011**, *61*, 167–232. [CrossRef]
15. Eliwa, H.A.; El-Bialy, M.Z.; Murata, M. Edicaran Post-Collisional Volcanism in the Arabian-Nubian Shield: The High-K Calc-Alkaline Dokhan Volcanics of Gabal Samr El-Qaa (592 ± 5 Ma), North Eastern Desert, Egypt. *Precambrian Res.* **2014**, *246*, 180–207. [CrossRef]
16. Mansour, S.E.E. Long-Term Topographic Evolution of the African Plate, Causes and Consequences for Surrounding Lithospheric Plates. Ph.D. Thesis, Universität Heidelberg, Heidelberg, Germany, 2015.
17. Mansour, S.; Hasebe, N.; Azab, E.; Elnaggar, A.Y.; Tamura, A. Combined Zircon/Apatite U-Pb and Fission-Track Dating by LA-ICP-MS and Its Geological Applications: An Example from the Egyptian Younger Granites. *Minerals* **2021**, *11*, 1341. [CrossRef]
18. Omar, G.I.; Steckler, M.S.; Buck, W.R.; Kohn, B.P. Fission-Track Analysis of Basement Apatites at the Western Margin of the Gulf of Suez Rift, Egypt: Evidence for Synchroneity of Uplift and Subsidence. *Earth Planet. Sci. Lett.* **1989**, *94*, 316–328. [CrossRef]
19. Kohn, B.P.; Feinstein, S.; Foster, D.A.; Steckler, M.S.; Eyal, M. Thermal History of the Eastern Gulf of Suez, II. Reconstruction from Apatite Fission Track and K-Feldspar Measurements. *Tectonophysics* **1997**, *283*, 219–239. [CrossRef]
20. Kohn, B.P.; Eyal, M. History of Uplift of the Crystalline Basement of Sinai and Its Relation to Opening of the Red Sea as Revealed by Fission Track Dating of Apatites. *Earth Planet. Sci. Lett.* **1981**, *52*, 129–141. [CrossRef]
21. Vermeesch, P.; Avigad, D.; McWilliams, M.O. 500 m.y. of Thermal History Elucidated by Multi-Method Detrital Thermochronology of North Gondwana Cambrian Sandstone (Eilat Area, Israel). *GSA Bull.* **2009**, *121*, 1204–1216. [CrossRef]
22. Feinstein, S.; Eyal, M.; Kohn, B.P.; Steckler, M.S.; Ibrahim, K.M.; Moh'd, B.K.; Tian, Y. Uplift and Denudation History of the Eastern Dead Sea Rift Flank, SW Jordan: Evidence from Apatite Fission Track Thermochronometry. *Tectonics* **2013**, *32*, 1513–1528. [CrossRef]

23. Kolodner, K.; Avigad, D.; McWILLIAMS, M.; Wooden, J.L.; Weissbrod, T.; Feinstein, S. Provenance of North Gondwana Cambrian–Ordovician Sandstone: U–Pb SHRIMP Dating of Detrital Zircons from Israel and Jordan. *Geol. Mag.* **2006**, *143*, 367–391. [CrossRef]
24. Kohn, B.P.; Eyal, M.; Feinstein, S. A Major Late Devonian-Early Carboniferous (Hercynian) Thermotectonic Event at the NW Margin of the Arabian-Nubian Shield: Evidence from Zircon Fission Track Dating. *Tectonics* **1992**, *11*, 1018–1027. [CrossRef]
25. Stampfli, G.M.; von Raumer, J.F.; Borel, G.D. Paleozoic Evolution of Pre-Variscan Terranes: From Gondwana to the Variscan Collision. In *Variscan-Appalachian Dynamics: The Building of the Late Paleozoic Basement*; Geological Society of America: Boulder, CO, USA, 2002; ISBN 978-0-8137-2364-8.
26. Alsharhan, A.S.; Nairn, A.E.M. *Sedimentary Basins and Petroleum Geology of the Middle East*; Elsevier: Amsterdam, The Netherlands, 1997; ISBN 978-0-444-82465-3.
27. Meneisy, M.Y. Mesozoic Igneous Activity in Egypt. *Qatar Univ. Sci. Bull.* **1986**, *6*, 317–328.
28. Sakran, S.; Shehata, A.A.; Osman, O.; El-Sherbiny, M. Superposed Tectonic Regimes in West Beni Suef Basin, Nile Valley, Egypt: Implications to Source Rock Maturation and Hydrocarbon Entrapment. *J. Afr. Earth Sci.* **2019**, *154*, 1–19. [CrossRef]
29. Shehata, A.A.; El Fawal, F.M.; Ito, M.; Aboulmagd, M.A.; Brooks, H.L. Senonian Platform-to-Slope Evolution in the Tectonically-Influenced Syrian Arc Sedimentary Belt: Beni Suef Basin, Egypt—ScienceDirect. *J. Afr. Earth Sci.* **2020**, *170*, 103934. [CrossRef]
30. Yousif, M.; Hussien, H.M.; Abotalib, A.Z. The Respective Roles of Modern and Paleo Recharge to Alluvium Aquifers in Continental Rift Basins: A Case Study from El Qaa Plain, Sinai, Egypt. *Sci. Total Environ.* **2020**, *739*, 139927. [CrossRef]
31. Khalil, M.M.; Hamer, K.; Pichler, T.; Abotalib, A.Z. Fault Zone Hydrogeology in Arid Environments: The Origin of Cold Springs in the Wadi Araba Basin, Egypt. *Hydrol. Process.* **2021**, *35*, e14176. [CrossRef]
32. Barbarand, J.; Marques, F.O.; Hildenbrand, A.; Pinna-Jamme, R.; Nogueira, C.R. Thermal Evolution of Onshore West Iberia: A Better Understanding of the Ages of Breakup and Rift-to-Drift in the Iberia-Newfoundland Rift. *Tectonophysics* **2021**, *813*, 228926. [CrossRef]
33. Mansour, S.; Glasmacher, U.A.; Krob, F.C.; Casillas, R.; Albinger, M. Timing of Rapid Cooling and Erosional Decay of Two Volcanic Islands of the Canary Archipelago: Implications from Low-Temperature Thermochronology. *Int. J. Earth Sci.* **2022**, *112*, 345–382. [CrossRef]
34. Steckler, M.S. Uplift and Extension at the Gulf of Suez: Indications of Induced Mantle Convection. *Nature* **1985**, *317*, 135–139. [CrossRef]
35. Omar, G.I.; Kohn, B.P.; Lutz, T.M.; Faul, H. The Cooling History of Silurian to Cretaceous Alkaline Ring Complexes, South Eastern Desert, Egypt, as Revealed by Fission-Track Analysis. *Earth Planet. Sci. Lett.* **1987**, *83*, 94–108. [CrossRef]
36. Kroner, A.; Todt, W.; Hussein, I.; Mansour, M.; Rashwan, A. Dating of Late Proterozoic Ophiolites in Egypt and the Sudan Using the Single Grain Zircon Evaporation Technique. *Precambrian Res.* **1992**, *59*, 15–32. [CrossRef]
37. Omar, G.I.; Steckler, M.S. Fission Track Evidence on the Initial Rifting of the Red Sea: Two Pulses, No Propagation. *Science* **1995**, *270*, 1341–1344. [CrossRef]
38. Bojar, A.-V.; Fritz, H.; Kargl, S.; Unzog, W. Phanerozoic Tectonothermal History of the Arabian–Nubian Shield in the Eastern Desert of Egypt: Evidence from Fission Track and Paleostress Data. *J. Afr. Earth Sci.* **2002**, *34*, 191–202. [CrossRef]
39. Mansour, S.; Gharib, M.A.; Hasebe, N.; Abdelrahman, K.; Fnais, M.S.; Tamura, A. Tectonic Evolution of the Gabal Loman Area, North Eastern Desert, Egypt: Implications from Low-Temperature Multithermochronometry on the Arabian-Nubian Shield. *Front. Earth Sci.* **2023**, *11*, 1193692. [CrossRef]
40. Feinstein, S.; Kohn, B.P.; Steckler, M.S.; Eyal, M. Thermal History of the Eastern Margin of the Gulf of Suez, I. Reconstruction from Borehole Temperature and Organic Maturity Measurements. *Tectonophysics* **1996**, *266*, 203–220. [CrossRef]
41. Bosworth, W.; Stockli, D.F.; Helgeson, D.E. Integrated Outcrop, 3D Seismic, and Geochronologic Interpretation of Red Sea Dike-Related Deformation in the Western Desert, Egypt—The Role of the 23 Ma Cairo "Mini-Plume". *J. Afr. Earth Sci.* **2015**, *109*, 107–119. [CrossRef]
42. Hansen, S.E.; Nyblade, A.A.; Benoit, M.H. Mantle Structure beneath Africa and Arabia from Adaptively Parameterized P-Wave Tomography: Implications for the Origin of Cenozoic Afro-Arabian Tectonism. *Earth Planet. Sci. Lett.* **2012**, *319–320*, 23–34. [CrossRef]
43. Faccenna, C.; Becker, T.W.; Jolivet, L.; Keskin, M. Mantle Convection in the Middle East: Reconciling Afar Upwelling, Arabia Indentation and Aegean Trench Rollback. *Earth Planet. Sci. Lett.* **2013**, *375*, 254–269. [CrossRef]
44. Ebinger, C.J.; Sleep, N.H. Cenozoic Magmatism throughout East Africa Resulting from Impact of a Single Plume. *Nature* **1998**, *395*, 788–791. [CrossRef]
45. Szymanski, E.; Stockli, D.F.; Johnson, P.R.; Hager, C. Thermochronometric Evidence for Diffuse Extension and Two-Phase Rifting within the Central Arabian Margin of the Red Sea Rift. *Tectonics* **2016**, *35*, 2863–2895. [CrossRef]
46. Hay, W.W. Tectonics and Climate. *Geol. Rundsch.* **1996**, *85*, 409–437. [CrossRef]
47. Reiners, P. Past, Present, and Future of Thermochronology. *Rev. Mineral. Geochem.* **2005**, *58*, 1–18. [CrossRef]
48. Stalder, N.; Herman, F.; Fellin, M.; Coutand, I.; Aguilar, G.; Reiners, P.; Fox, M. The Relationships between Tectonics, Climate and Exhumation in the Central Andes (18–36°S): Evidence from Low-Temperature Thermochronology. *Earth-Sci. Rev.* **2020**, *210*, 103276. [CrossRef]
49. Ott, R.; Gallen, S.F.; Helman, D. Erosion and Weathering in Carbonate Regions Reveal Climatic and Tectonic Drivers of Carbonate Landscape Evolution. *Earth Surf. Dyn.* **2023**, *11*, 247–257. [CrossRef]

50. Gleadow, A.J.W.; Duddy, I.R.; Lovering, J.F. Fission Track Analysis: A New Tool Fo the Evaluation of Thermal Histories and Hydrocarbon Potential. *APPEA J.* **1983**, *23*, 93. [CrossRef]
51. Green, P.F.; Duddy, I.R.; Laslett, G.M.; Hegarty, K.A.; Gleadow, A.J.W.; Lovering, J.F. Thermal Annealing of Fission Tracks in Apatite 4. Quantitative Modelling Techniques and Extension to Geological Timescales. *Chem. Geol. Isot. Geosci. Sect.* **1989**, *79*, 155–182. [CrossRef]
52. Lambiase, J.J.; Morley, C.K. Hydrocarbons in Rift Basins: The Role of Stratigraphy. *Philos. Trans. R. Soc. Lond. Ser. A Math. Phys. Eng. Sci.* **1999**, *357*, 877–900. [CrossRef]
53. Abotalib, A.Z.; Heggy, E.; El Bastawesy, M.; Ismail, E.; Gad, A.; Attwa, M. Groundwater Mounding: A Diagnostic Feature for Mapping Aquifer Connectivity in Hyper-Arid Deserts. *Sci. Total Environ.* **2021**, *801*, 149760. [CrossRef]
54. Attwa, M.; El Bastawesy, M.; Ragab, D.; Othman, A.; Assaggaf, H.M.; Abotalib, A.Z. Toward an Integrated and Sustainable Water Resources Management in Structurally-Controlled Watersheds in Desert Environments Using Geophysical and Remote Sensing Methods. *Sustainability* **2021**, *13*, 4004. [CrossRef]
55. Sahour, H.; Sultan, M.; Abdellatif, B.; Emil, M.; Abotalib, A.; Abdelmohsen, K.; Vazifedan, M.; Mohammad, A.; Hassan, S.; Roshdy, M.; et al. Identification of Shallow Groundwater in Arid Lands Using Multi-Sensor Remote Sensing Data and Machine Learning Algorithms. *J. Hydrol.* **2022**, *614*, 128509. [CrossRef]
56. Jones, D.K.C. Ground Conditions and Hazards: Suez City Development, Egypt. In *Land Surface Evaluation for Engineering Practice*; Griffiths, J.S., Ed.; Geological Society of London: London, UK, 2001; Volume 18, p. 279, ISBN 978-1-86239-084-3.
57. Aboulela, H.A.; Arnous, M.O. Geo-Hazards Assessment of Western Adabyia Port Area, Gulf of Suez, Egypt. *CATRINA* **2008**, *3*, 65–78.
58. Watchorn, F.; Nichols, G.J.; Bosence, D.W.J. Rift-Related Sedimentation and Stratigraphy, Southern Yemen (Gulf of Aden). In *Sedimentation and Tectonics in Rift Basins Red Sea:- Gulf of Aden*; Purser, B.H., Bosence, D.W.J., Eds.; Springer: Dordrecht, The Netherlands, 1998; pp. 165–189, ISBN 978-94-010-6068-4.
59. Leroy, S.; Razin, P.; Autin, J.; Bache, F.; d'Acremont, E.; Watremez, L.; Robinet, J.; Baurion, C.; Denèle, Y.; Bellahsen, N.; et al. From Rifting to Oceanic Spreading in the Gulf of Aden: A Synthesis. *Arab. J. Geosci.* **2012**, *5*, 859–901. [CrossRef]
60. Pik, R.; Bellahsen, N.; Leroy, S.; Denèle, Y.; Razin, P.; Ahmed, A.; Khanbari, K. Structural Control of Basement Denudation during Rifting Revealed by Low-Temperature (U–Th–Sm)/He Thermochronology of the Socotra Island Basement—Southern Gulf of Aden Margin. *Tectonophysics* **2013**, *607*, 17–31. [CrossRef]
61. Serra-Kiel, J.; Gallardo-Garcia, A.; Razin, P.; Robinet, J.; Roger, J.; Grelaud, C.; Leroy, S.; Robin, C. Middle Eocene-Early Miocene Larger Foraminifera from Dhofar (Oman) and Socotra Island (Yemen). *Arab. J. Geosci.* **2016**, *9*, 344. [CrossRef]
62. Hempton, M.R. Structure and Deformation History of the Bitlis Suture near Lake Hazar, Southeastern Turkey. *Geol. Soc. Am. Bull.* **1985**, *96*, 233. [CrossRef]
63. Bosworth, W.; Huchon, P.; McClay, K. The Red Sea and Gulf of Aden Basins. *J. Afr. Earth Sci.* **2005**, *43*, 334–378. [CrossRef]
64. Hofmann, C.; Courtillot, V.; Féraud, G.; Rochette, P.; Yirgu, G.; Ketefo, E.; Pik, R. Timing of the Ethiopian Flood Basalt Event and Implications for Plume Birth and Global Change. *Nature* **1997**, *389*, 838–841. [CrossRef]
65. George, R.; Rogers, N.; Kelley, S. Earliest Magmatism in Ethiopia: Evidence for Two Mantle Plumes in One Flood Basalt Province. *Geology* **1998**, *26*, 923. [CrossRef]
66. Bosworth, W.; Stockli, D.F. Early Magmatism in the Greater Red Sea Rift: Timing and Significance. *Can. J. Earth Sci.* **2016**, *53*, 1158–1176. [CrossRef]
67. Rooney, T.O. The Cenozoic Magmatism of East-Africa: Part I—Flood Basalts and Pulsed Magmatism. *Lithos* **2017**, *286–287*, 264–301. [CrossRef]
68. Cole, G.A.; Abu-Ali, M.A.; Coiling, E.L.; Halpern, H.I.; Carrigan, W.J.; Savage, G.R.; Scolaro, R.J.; AI-Sharidi, S.H. Petroleum geochemistry of the Midyan and Jaizan basins of the Red Sea, Saudi Arabia. *Mar. Pet. Geol.* **1995**, *12*, 597–614. [CrossRef]
69. ArRajehi, A.; McClusky, S.; Reilinger, R.; Daoud, M.; Alchalbi, A.; Ergintav, S.; Gomez, F.; Sholan, J.; Bou-Rabee, F.; Ogubazghi, G.; et al. Geodetic Constraints on Present-day Motion of the Arabian Plate: Implications for Red Sea and Gulf of Aden Rifting. *Tectonics* **2010**, *29*, 2009TC002482. [CrossRef]
70. Stab, M.; Bellahsen, N.; Pik, R.; Quidelleur, X.; Ayalew, D.; Leroy, S. Modes of Rifting in Magma-Rich Settings: Tectono-Magmatic Evolution of Central Afar: Modes of Rifting in Magma-Rich Settings. *Tectonics* **2016**, *35*, 2–38. [CrossRef]
71. Kröner, A.; Kröger, J.; Rashwan, A.A.A. Age and Tectonic Setting of Granitoid Gneisses in the Eastern Desert of Egypt and South-West Sinai. *Geol. Rundsch.* **1994**, *83*, 502–513. [CrossRef]
72. Stern, R.J.; Hedge, C.E. Geochronologic and Isotopic Constraints on Late Precambrian Crustal Evolution in the Eastern Desert of Egypt. *Am. J. Sci.* **1985**, *285*, 97. [CrossRef]
73. Khedr, M.Z.; Abo Khashaba, S.M.; El-Shibiny, N.H.; El-Arafy, R.A.; Takazawa, E.; Azer, M.K.; Palin, R.M. Remote Sensing Techniques and Geochemical Constraints on the Formation of the Wadi El-Hima Mineralized Granites, Egypt: New Insights into the Genesis and Accumulation of Garnets. *Int. J. Earth Sci.* **2022**, *111*, 2409–2443. [CrossRef]
74. Platt, J.P.; England, P.C. Convective Removal of Lithosphere beneath Mountain Belts; Thermal and Mechanical Consequences. *Am. J. Sci.* **1994**, *294*, 307–336. [CrossRef]
75. Abo Khashaba, S.; El-Shibiny, N.H.; Hassan, S.; Takazawa, E.; Khedr, M. Application of Remote Sensing Data Integration in Detecting Mineralized Granitic Zones: A Case Study of the Gabal Al-Ijlah Al-Hamra, Central Eastern Desert, Egypt. *J. Afr. Earth Sci.* **2023**, *200*, 104855. [CrossRef]

76. Said, R. *The Geology of Egypt*, 2nd ed.; A.A. Balkema: Rotterdam, The Netherlands, 1990.
77. Klitzsch, E. Plate Tectonics and Cratonal Geology in Northeast Africa (Egypt, Sudan). *Geol. Rundsch.* **1986**, *75*, 755–768. [CrossRef]
78. Klitzsch, E. Paleozoic. In *The Geology of Egypt*; Said, R., Ed.; A.A. Balkema: Rotterdam, The Netherlands, 1990; Volume 24, pp. 451–486.
79. Moustafa, A.R.; Yousif, M.S.M. Structural Evolution of the Eastern Shoulder of the Suez Rift: Um Bogma Area. *Neues Jahrb. Geol. Paläontol. Monatshefte* **1993**, *1993*, 655–668. [CrossRef]
80. Elhebiry, M.; Sultan, M.; Abotalib, A.; Kehew, A.; Voice, P.; El-Leil, I. Red Sea Tectonics Unveil the Largest Known Terrestrial Ice Stream: New Constraints on Late Ordovician Ice Sheet Dynamics. *Earth Planet. Sci. Lett.* **2021**, *587*, 117531. [CrossRef]
81. Dewey, J.F.; Pitman, W.C.; Ryan, W.B.F.; Bonnin, J. Plate Tectonics and the Evolution of the Alpine System. *Geol. Soc. Am. Bull.* **1973**, *84*, 3137. [CrossRef]
82. Girdler, R.W. Problems Concerning the Evolution of Oceanic Lithosphere in the Northern Red Sea. *Tectonophysics* **1985**, *116*, 109–122. [CrossRef]
83. Wagner, G.A. Spaltspurenalter von Mineralen Und Natürlichen Gläsern: Eine Übersicht. *Fortschritte Mineral.* **1972**, *49*, 114–145.
84. Gleadow, A.J.W.; Duddy, I.R. A Natural Long-Term Track Annealing Experiment for Apatite. *Nucl. Tracks* **1981**, *5*, 169–174. [CrossRef]
85. Yamada, R.; Tagami, T.; Nishimura, S.; Ito, H. Annealing Kinetics of Fission Tracks in Zircon: An Experimental Study. *Chem. Geol.* **1995**, *122*, 249–258. [CrossRef]
86. Morishita, T.; Ishida, Y.; Arai, S.; Shirasaka, M. Determination of Multiple Trace Element Compositions in Thin (>30 μM) Layers of NIST SRM 614 and 616 Using Laser Ablation-Inductively Coupled Plasma-Mass Spectrometry (LA-ICP-MS). *Geostand. Geoanal. Res.* **2005**, *29*, 107–122. [CrossRef]
87. Garver, J.I. Etching Zircon Age Standards for Fission-Track Analysis. *Radiat. Meas.* **2003**, *37*, 47–53. [CrossRef]
88. Vermeesch, P. IsoplotR: A Free and Open Toolbox for Geochronology. *Geosci. Front.* **2018**, *9*, 1479–1493. [CrossRef]
89. Longerich, H.P.; Jackson, S.E.; Günther, D. Inter-Laboratory Note. Laser Ablation Inductively Coupled Plasma Mass Spectrometric Transient Signal Data Acquisition and Analyte Concentration Calculation. *J. Anal. At. Spectrom.* **1996**, *11*, 899–904. [CrossRef]
90. Carpenter, B.S.; Reimer, G.M. Standard Reference Materials: Calibrated Glass Standards for Fission Track Use. 1974. Available online: https://nvlpubs.nist.gov/nistpubs/Legacy/SP/nbsspecialpublication260-49.pdf (accessed on 29 July 2023).
91. Pearce, N.J.G.; Perkins, W.T.; Westgate, J.A.; Gorton, M.P.; Jackson, S.E.; Neal, C.R.; Chenery, S.P. A Compilation of New and Published Major and Trace Element Data for NIST SRM 610 and NIST SRM 612 Glass Reference Materials. *Geostand. Geoanal. Res.* **1997**, *21*, 115–144. [CrossRef]
92. Barbarand, J.; Carter, A.; Wood, I.; Hurford, T. Compositional and Structural Control of Fission-Track Annealing in Apatite. *Chem. Geol.* **2003**, *198*, 107–137. [CrossRef]
93. Ketcham, R.A. Forward and Inverse Modeling of Low-Temperature Thermochronometry Data. *Rev. Mineral. Geochem.* **2005**, *58*, 275–314. [CrossRef]
94. Ketcham, R.A. *HeFTy*, Version 1.6.7; Apatite to Zircon, Inc.: Viola, ID, USA, 2009.
95. Morgan, P.; Boulos, F.K.; Hennin, S.F.; El-Sherif, A.A.; El-Sayed, A.A.; Basta, N.Z.; Melek, Y.S. Heat Flow in Eastern Egypt: The Thermal Signature of a Continental Breakup. *J. Geodyn.* **1985**, *4*, 107–131. [CrossRef]
96. Donelick, R.A.; O'Sullivan, P.B.; Ketcham, R.A. 3. Apatite Fission-Track Analysis. In *Low-Temperature Thermochronology*; Reiners, P.W., Ehlers, T.A., Eds.; De Gruyter: Berlin, Germany; Boston, MA, USA, 2005; pp. 49–94, ISBN 978-1-5015-0957-5.
97. Bernet, M.; Brandon, M.; Garver, J.; Balestieri, M.L.; Ventura, B.; Zattin, M. Exhuming the Alps through Time: Clues from Detrital Zircon Fission-Track Thermochronology. *Basin Res.* **2009**, *21*, 781–798. [CrossRef]
98. Klitzsch, E.; Wycisk, P. Geology of the Sedimentary Basins of Northern Sudan and Bordering Areas. *Berl. Geowiss. Abh. Reihe A Geol. Palaeontol.* **1987**, *75*, 97–136.
99. Gleadow, A.J.W.; Duddy, I.R.; Green, P.F.; Lovering, J.F. Confined Fission Track Lengths in Apatite: A Diagnostic Tool for Thermal History Analysis. *Contrib. Mineral. Petrol.* **1986**, *94*, 405–415. [CrossRef]
100. Tewfik, N.; Harwood, C.; Deighton, I. The Miocene, Rudeis and Kareem Formations in the Gulf of Suez: Aspects of Sedimentology and Geochemistry. In Proceedings of the 11th Petroleum Exploration and Production Conference, Cairo, Egypt, 7–10 November 1992; Volume 11, pp. 84–113.
101. Darwish, M.; El Araby, A. Petrography and Diagenetic Aspects of Some Siliclastic Hydrocarbon Reservoirs in Relation to Rifting of the Gulf of Suez, Egypt. Geodynamics and Sedimentation of the Red Sea—Gulf of Aden Rift System. *Egypt. J. Geol.* **1994**, *3*, 1–25.
102. Ketcham, R.A.; Donelick, R.A.; Balestrieri, M.L.; Zattin, M. Reproducibility of Apatite Fission-Track Length Data and Thermal History Reconstruction. *Earth Planet. Sci. Lett.* **2009**, *284*, 504–515. [CrossRef]
103. Gvirtzman, G.; Weissbrod, T. The Hercynian Geanticline of Helez and the Late Palaeozoic History of the Levant. *Geol. Soc. Lond. Spec. Publ.* **1984**, *17*, 177–186. [CrossRef]

104. Seilacher, A. Paleozoic Trace Fossils. In *Geology of Egypt*; A.A. Balkema: Rotterdam, The Netherlands, 1990; pp. 113–156.
105. Moustafa, A.R.; Fouda, H.G.A. Structural Architecture and Tectonic Evolution of the Yelleg Inverted Half Graben, Northern Sinai, Egypt. *Mar. Pet. Geol.* **2014**, *51*, 286–297. [CrossRef]